

Supplementary Information: Kinetic Versus Thermodynamic Polymorph Stabilization of a Tri-Carboxylic Acid Derivative at the Solid-Liquid Interface

Richa Arjariya,[†] Gagandeep Kaur,[†] Shantanu Sen,[†] Sandeep Verma,[†] Markus
Lackinger,^{‡,¶} and Thiruvancheril G. Gopakumar^{*,†}

[†]*Department of Chemistry, Indian Institute of Technology Kanpur, Kanpur, UP-208016,
India*

[‡]*Department of Physics, Technical University of Munich, James-Franck-Strasse 1,
Garching 85748, Germany*

[¶]*Deutsches Museum, Museumsinsel 1, Munich 80538, Germany*

E-mail: gopan@iitk.ac.in

Phone: +91 5122596830. Fax: +91 5122596806

S1: Synthesis and characterization of L-BTA molecule

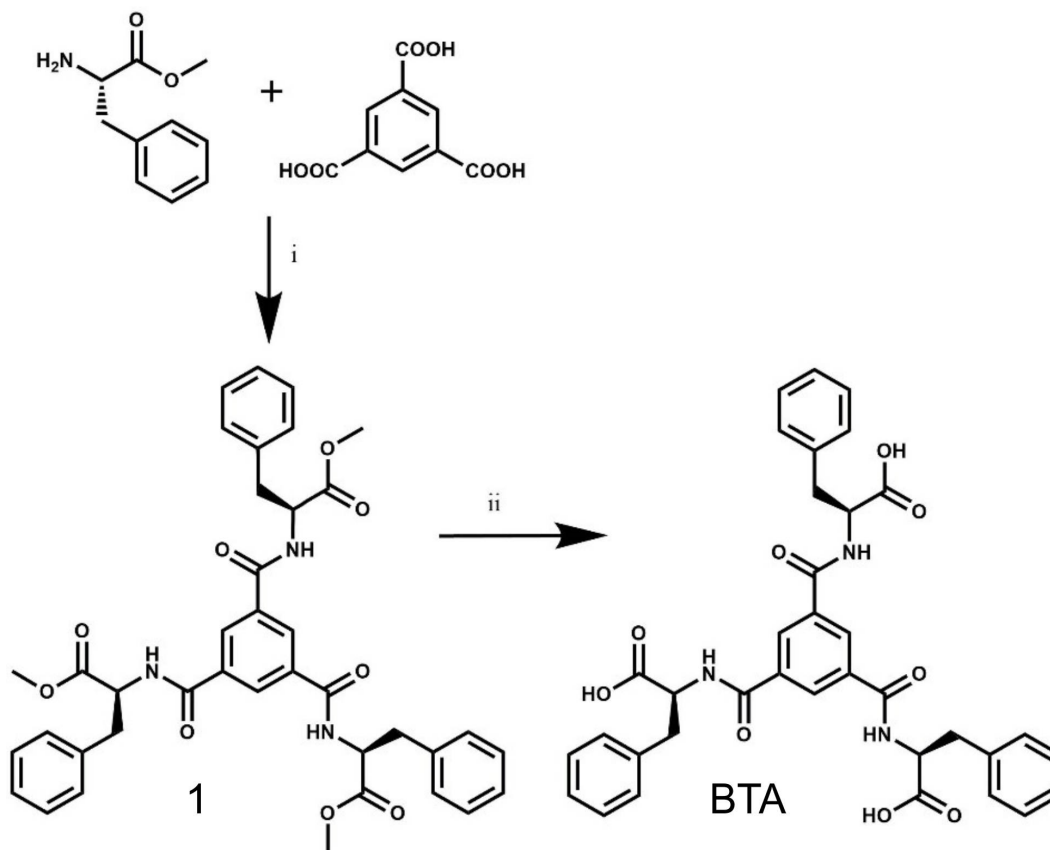


Figure 1: Scheme of solution phase synthesise of BTA.

Trimesic acid tris L-phenylalanine methyl ester conjugate (1):

Compound 1 (Trimesic acid tris L-phenylalanine methyl ester conjugate) was synthesized from trimesic acid and L-phenylalanine methyl ester. Trimesic acid (0.50g, 2.37mmol), and Hydroxybenzotriazole (HOBt) were dissolved in dry N, N Dimethylformamide (DMF) (15 mL) under nitrogen atmosphere and the reaction mixture was cooled to 0°C in an ice bath. A solution of N, N Dicyclohexylcarbodiimide (DCC) in Dichloromethane (DCM) (1.47g, 7.13mmol) was then added drop-wise to the reaction mixture. The reaction mixture was stirred at 0°C for 1 h, after which, L-phenylalanine methyl ester (1.63g, 7.58mmol) was added to it followed by triethylamine (2.313mL, 16.5mmol). The reaction mixture was monitored and stirred for 24 h at room temperature under nitrogen atmosphere. The reaction mixture was concentrated in vacuo, redissolved in ethyl acetate and filtered to remove Dicyclohexylurea (DCU). The organic layer was then washed with 1N HCl (3·30 mL), 10% NaHCO₃ (3·30 mL) and brine (30 mL). The organic layer was dried over anhydrous sodium sulfate and concentrated in vacuo. The crude compound was purified by silica gel column chromatography by using DCM and methanol (98:2) solvent system to isolate pure 1. The ¹HNMR and ¹³CNMR of compound 1 are shown in Figure 2. Other details are provided below.

Yield: 72%(0.365 g).

Melting point: 199-203°C

Rf [4% methanol in DCM]: 0.5

¹HNMR : (400 MHz, DMSO-d₆) δ (ppm): 9.11–9.14 (m, 3H), 8.33 (s, 3H), 7.15–7.26 (m, 15H), 4.64–4.69 (m, 3H), 3.61 (s, 9H), 3.06–3.16 (m, 6H).

¹³CNMR: (125 MHz; DMSO-d₆) δ (ppm): 172.5, 166.1, 134.7, 129.5, 128.8, 127.0, 54.9, 52.5, 37.8.

L-Benzene-1,3,5-tricarbonyl phenylalanine (L-BTA):

Compound 1 (0.1 g, 0.144 mmol) was dissolved in methanol to form a clear solution. To this 6N NaOH (0.03 g, 0.865mmol) was added and stirred for 6 h at room temperature. The solution obtained was passed over activated cation exchange resin. The filtrate was evaporated under reduced pressure to obtain pure BTA. The ^1H NMR and ^{13}C NMR of BTA are shown in Figure 3. The NMR spectra of L-BTA clearly shows that no diastereomers are formed and therefore all the three amino acid units in the final molecule should have the same chirality. Other details are provided below.

Yield: 72.9%(0.07 g).

^1H NMR: (400 MHz, DMSO- d_6) δ (ppm): 12.82 (br s, 3H), 8.97 (d, $J = 8.04$ Hz, 3H), 8.31 (s, 3H), 7.30–7.16 (m, 15H), 4.68-4.62 (m, 3H), 3.21–3.04 (m, 6H)

^{13}C NMR: (125 MHz; DMSO- d_6) δ (ppm): 173.5, 166.1, 138.6, 134.9, 129.5, 128.8, 126.9, 54.9, 36.8.

HRMS ($M+H$) $^+$ for $C_{36}H_{34}N_3O_9^+$: 652.2290 (calcd.), 652.2296 (Anal.), see Figure 4.

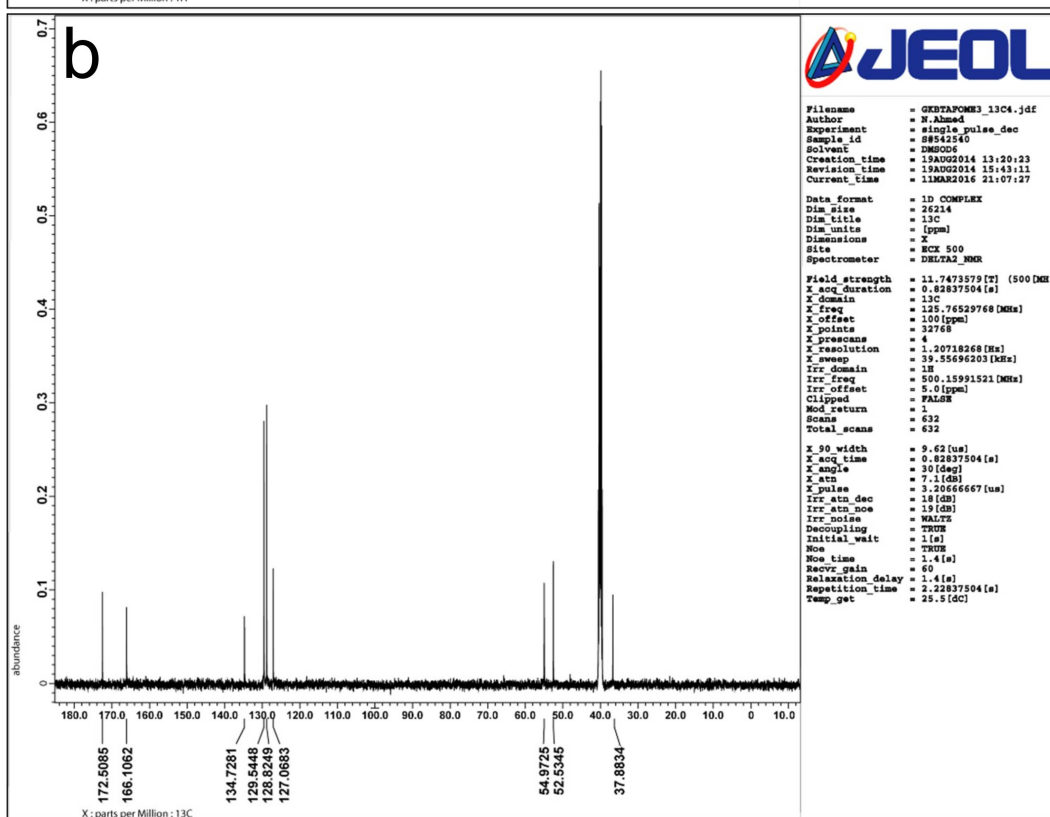
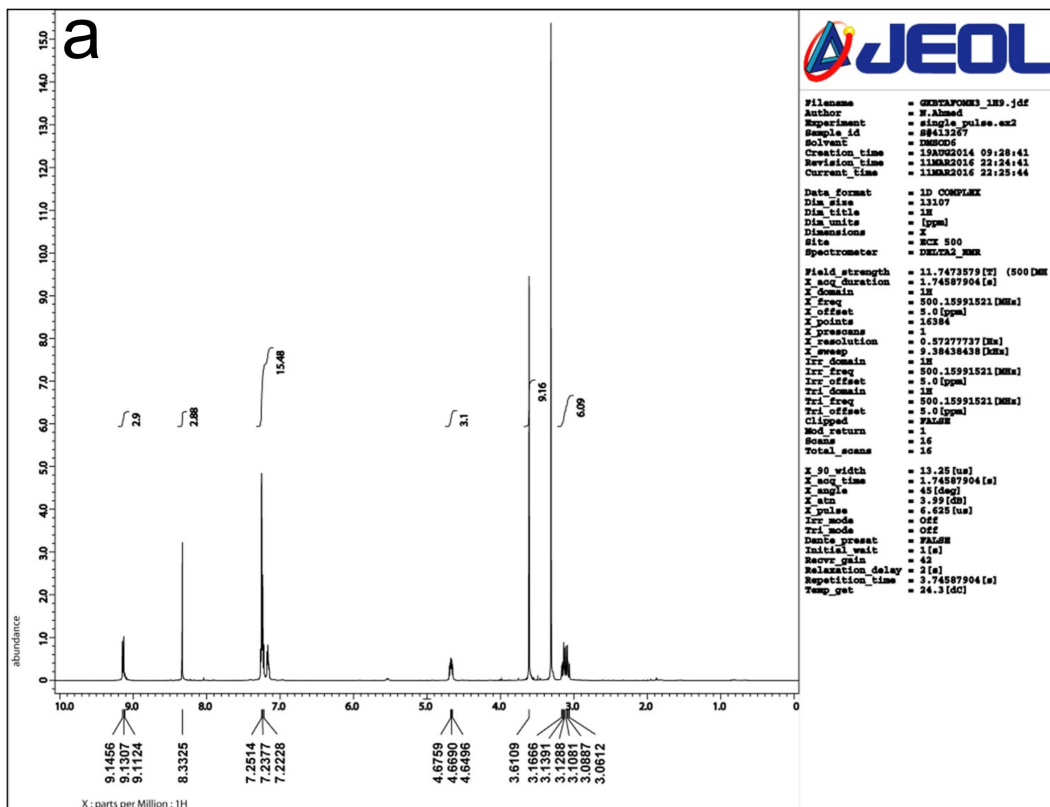


Figure 2: ^1H (a) and ^{13}C (b) NMR spectra of compound 1.

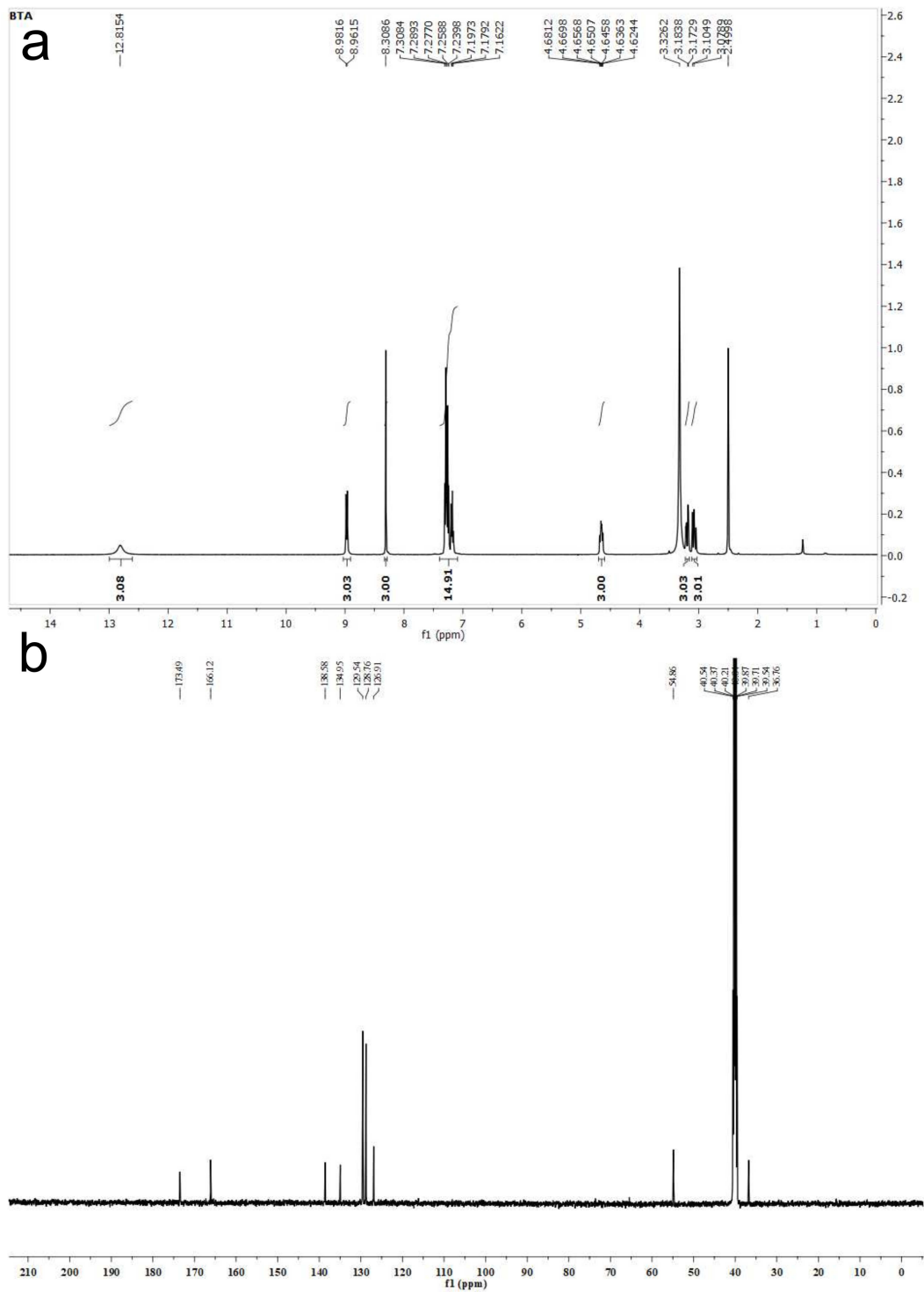


Figure 3: 1H (a) and ^{13}C (b) NMR spectra of L-BTA.

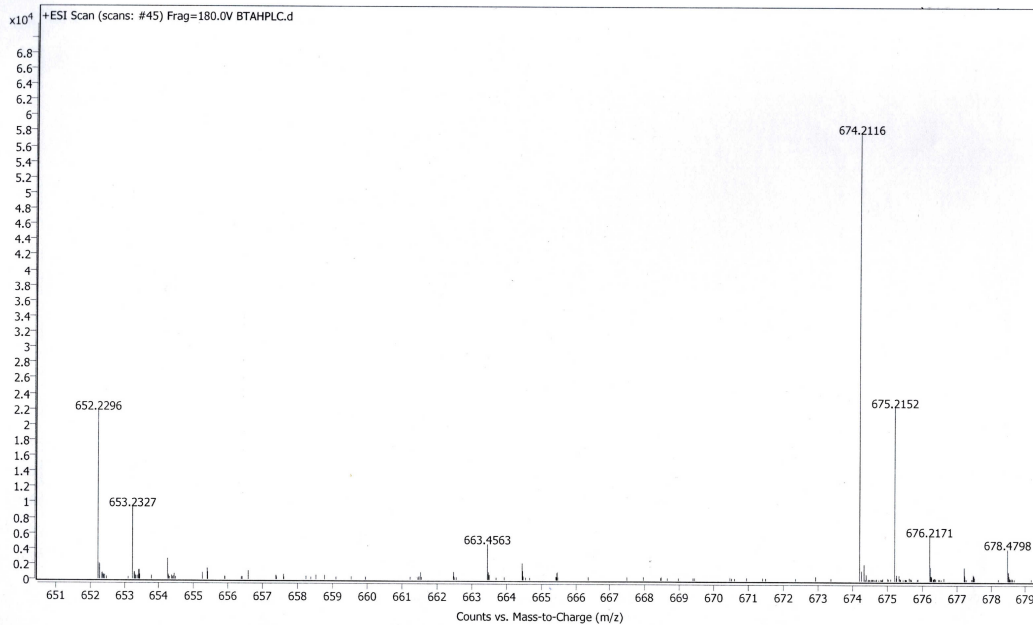


Figure 4: Mass spectrum obtained for L-BTA.

Circular dichroism spectroscopy of L-BTA:

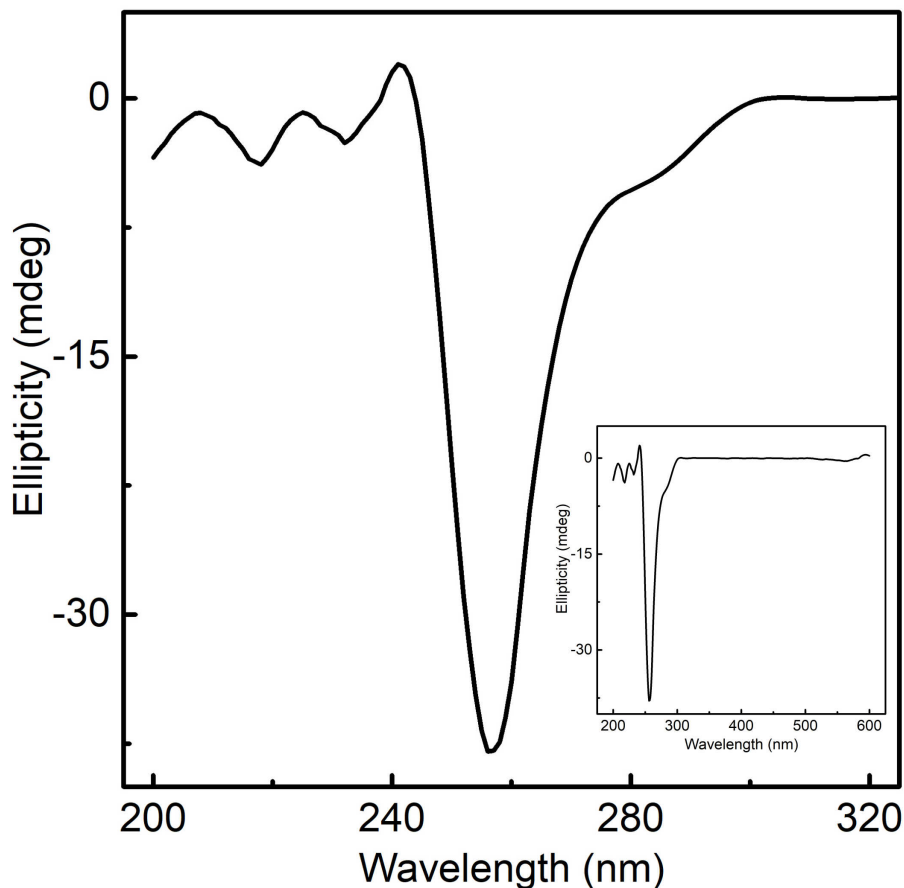


Figure 5: Averaged (3 times) circular dichroism spectrum of L-BTA.

Freshly prepared solution of BTA with a concentration of 5×10^{-3} M was prepared in HPLC grade methanol. CD spectrum (Figure 5) was recorded at room temperature using JASCO J-815 CD spectrometer and a quartz glass of 1 mm path length. To avoid any instrumental baseline drift contributed by the working solution, the background values were subtracted from each individual sample measurement. The spectrum obtained for L-BTA is in good agreement for the CD spectrum reported for the same compound (H_3L).¹ The agreement of λ minimum value (260 nm) is matching well with the report¹ suggesting the formation of L-enantiomer and thus low racemization. The specific rotation of L-BTA is -60° as characterized by polarimetry.

S2: Optimized geometry of SF structure of L-BTA

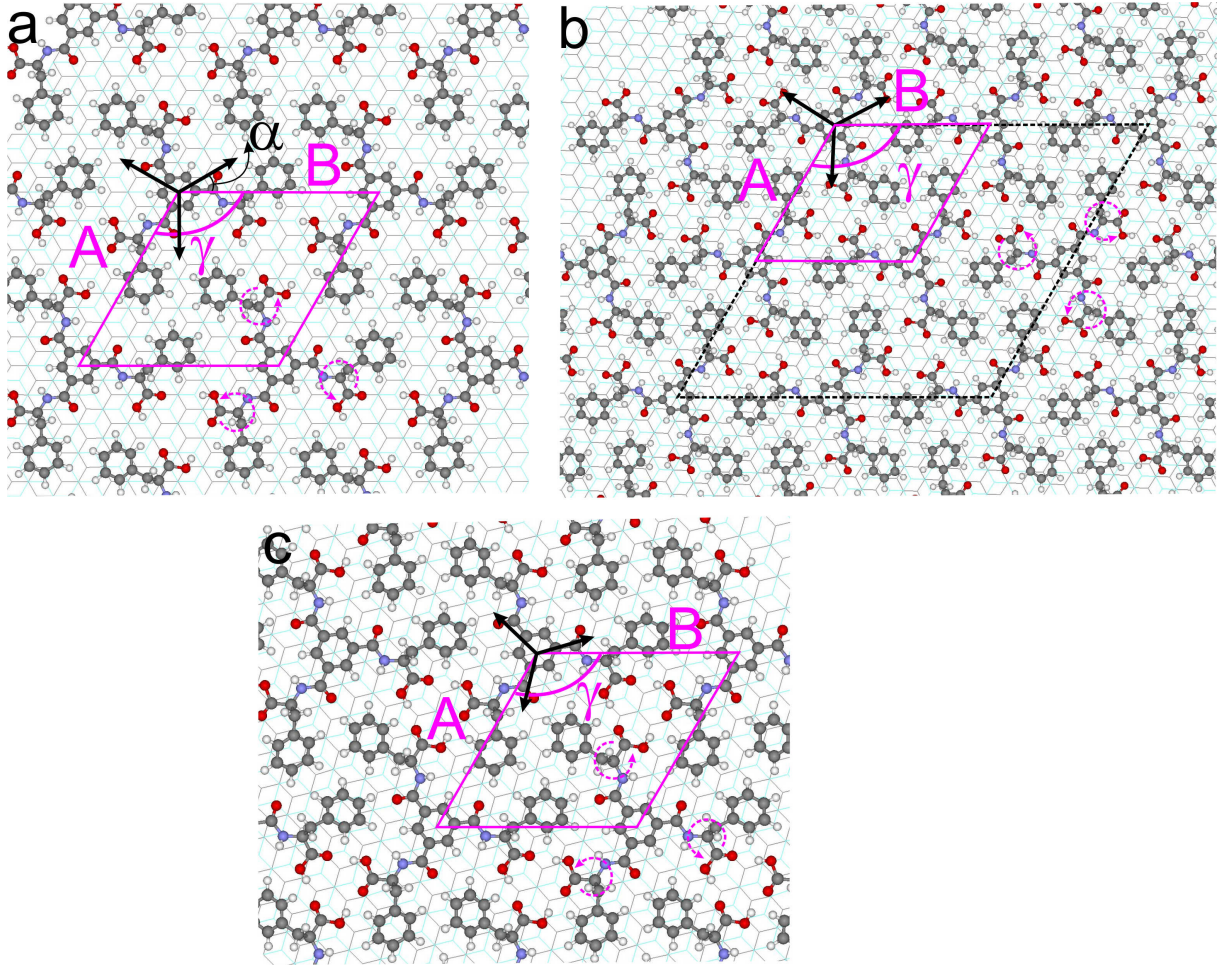


Figure 6: Force-field optimized geometry of possible SF structures of L-BTA on bilayer graphite. Black arrows indicate the high symmetry directions of graphite and magenta oblique shows the unit cell of SF pattern. The orientation of the molecular lattice with respect to graphite lattice direction (indicated as α) is different in different models; 30° (SF₃₀, a), 27.5° (SF₂₈, b) and 17.4° (SF₁₇, c). **A** and **B** are the molecular unit lattice vectors and γ is the angle between them. For SF₂₈ the unit cell for the simulation is 2×2 (marked by black dashed oblique) and for all others the cell is 1×1 (marked by magenta oblique).

To understand the relative binding energy of SF and CW structure, force-field calculation² has been carried out. Several possible input geometries (unit cell/commensurate cell) of SF and CW structures are considered near to the experimental lattice parameters. The optimized SF/CW geometries that are comparable to the experiments are listed in Tables 1 and 2. **A** and **B** are the unit lattice vectors of SF structure and γ is the angle between them. α is the angle between the graphite lattice direction and the molecular compact lattice direction. The average H-bond distance in 3-fold (SF) and 2-fold (CW) cyclic hydrogen bonding ($-\text{O}-\text{H}\cdots\text{O}-$) and the average H-bond distance between carbonyl group and aromatic hydrogen ($-\text{C}=\text{O}\cdots\text{H}-\text{C}-$) in SF are included in table. The optimized geometries of SF and CW are shown in Figures 6 and 7, respectively. The orientation of the molecular lattice with respect to graphite lattice direction (defined as α) is different in different models; 17.40° (SF₁₇, Figure 6a), 27.50° (SF₂₈, Figure 6b), 30° (SF₃₀, Figure 6c), 9.9° (CW₁₀, Figure 7a) and 0° (CW₀, Figure 7b). The binding energy (ΔE_{bind}) and adsorption energy (E_{ads}) of optimized models are also included in the table. ΔE_{bind} and E_{ads} are defined as follows,

$$\Delta E_{bind} = E_{BTA-SF/CW} - n \times E_{BTA-gas} \quad (1)$$

where, $E_{BTA-SF/CW}$ is the total energy of the molecule in the optimized SF or CW structure and $E_{BTA-gas}$ is the total energy of fully optimized molecule in gas phase. The gas phase geometry of BTA used for the calculation is similar to the geometry in both SF and CW.

$$E_{ads} = (E_{total} - E_{graphite}) - n \times E_{BTA-gas} \quad (2)$$

where, E_{total} is the total energy of BTA in optimized SF or CW structure on bilayer graphite, $E_{graphite}$ is the total energy of graphite in the cell. n is the number of molecules within the cell. ΔE_{bind} accounts for the molecule-molecule interaction and E_{ads} accounts the overall stability of the structure on surface. Larger magnitude of ΔE_{bind} and E_{ads} corresponds to energetically more favorable case. The ΔE_{bind} and E_{ads} values shown in Tables 1 and 2

correspond to energy per L-BTA molecule.

Table 1: Geometrical parameters of optimized SF structures on bilayer graphite.

SF	A, B, γ	α	E_{ads} (eV)	ΔE_{bind} (eV)	$-\text{O}-\text{H}\cdots\text{O}-$ (Å)	$-\text{C}=\text{O}\cdots\text{H}-\text{C}-$ (Å)
SF ₃₀	17.10, 17.10, 60.0°	30.0°	-3.42018	-0.09871	3.57	4.07
SF ₂₈	15.99, 15.99, 60.0°	27.5°	-4.1076	-0.77035	2.54	2.36
SF ₁₇	15.38, 15.38, 60°	17.4°	-3.3207	-0.7774	2.09	2.11
Expt.	15.7, 15.7, 60°	$\approx 30^\circ$				

SF₂₈ is the energetically most favorable case and resemblance closest to the experimental lattice parameters (**A**, **B**, γ and α). Though the experimental lattice parameters are matching for SF₁₇, α is not in agreement with the experiments. Even though, the average hydrogen bond distances in SF₁₇ are lower compared to SF₂₈, the E_{bind} in comparable to SF₂₈. We presume that the slight close-packing in SF₁₇ compared to SF₂₈ is possibly causing large steric repulsion within the pattern. Similarly, E_{ads} is lower for this case suggesting a non favorable adsorption with graphite. The lattice parameters in SF₃₀ is much larger than the experimental observation, though α is in agreement with experiment. Similarly, ΔE_{bind} and E_{ads} are lower for SF₃₀ compared to that of SF₂₈ and SF₁₇. Thus, we conclude that the adsorption geometry of L-BTA on graphite resembles the most to SF₂₈. In all the cases we have considered commensurate 1×1 or 2×2 cell for the calculation. Other super-cells may be considered to reproduce the experimental geometrical parameters.

Parameter set used for the calculation is as follows, Method: ReaxFF-CHO-2008; Force tolerance: 0.001 eV/Å; F stress tolerance: 0.001 eV/Å; Max step size: 0.01 Å; Optimizer method: LBFGS (Limited memory BFGS (L-BFGS)), which is an optimization algorithm in the family of quasi-Newton that approximates the Broyden-Fletcher-Goldfrab-Shanno (BFGS) algorithm using a limited amount of computer memory. A pre-optimized bilayer layer graphite was used from the library data as provided in the Quantumwise DFT package and was frozen during the optimization. The lattice parameter for the graphite are: $\vec{a} = 2.4612 \text{ Å}$, $\vec{b} = 2.4612 \text{ Å}$, $\vec{c} = 6.709 \text{ Å}$, and $\gamma = 60^\circ$.

S3: Optimized geometry of CW structure of L-BTA

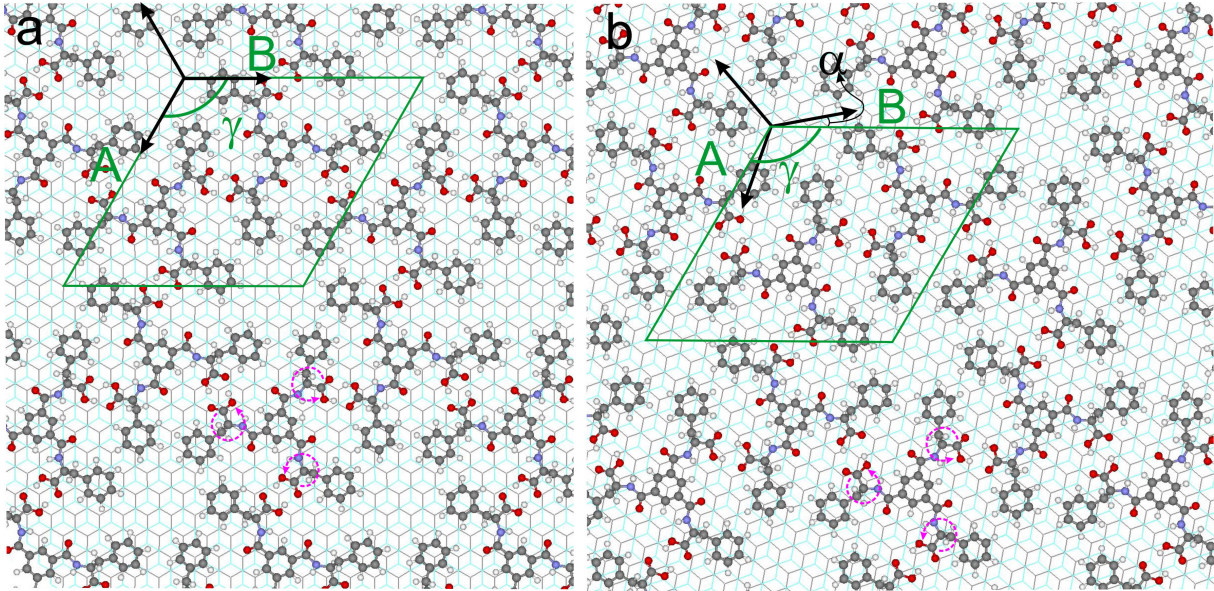


Figure 7: Force-field optimized geometry of CW structure of L-BTA on bilayer graphite. The orientation of the molecular lattice with respect to graphite lattice direction (indicated as α) is different in different models; 0° (CW_0 , a) and 9.9° (CW_{10} , b). **A** and **B** are the molecular lattice vectors and γ is the angle between them. Black arrows indicate the high symmetry directions of graphite and α is the angle between graphite and molecular compact lattice directions. Both CW_0 and CW_{10} , the unit cell for the simulation is 1×1 (marked by green oblique).

Force-field optimized geometric parameters, average H-bond distance, ΔE_{bind} and E_{ads} of CW_0 and CW_{10} are listed in Table 2. Though the lattice parameters of both CW_0 and CW_{10} are comparable to the experiments, α is matching only for CW_0 . For both cases ΔE_{bind} and E_{ads} are comparable and thus we finalize CW_0 as the final geometry for the observed CW structure. The comparison between SF and CW structure shows that binding energy per molecule of SF is higher than CW (12.5 kJ/mol). It is reported for unsubstituted trimesic acid derivatives that the binding energy per H-bond of 2-fold cyclic H-bonds is larger than that in 3-fold cyclic H-bonds (≈ 3.7 kJ/mol).³ The phenylalanine substituent of BTA gives not only rise to additional van-der-Waals interactions, but also facilitate additional intermolecular H-bonds (highlighted in Figure 1d) that are not feasible in the self-assembly of unsubstituted trimesic acid. The stronger binding energy per molecule in SF of L-BTA

translates into an even larger enthalpy per unit area ($\Delta h = \Delta H / \text{unit area}$) due to the higher packing density of SF as compared to CW. As the total entropy cost per molecule for adsorption from solution in the monolayer scales with the molecular packing density, SF structure has the highest entropy cost. That is, even when the binding energy is relatively high for SF structure, due to large entropy cost the overall formation free energy of SF pattern may be lower than CW pattern. Though the SF structure is spontaneously formed, it is dynamically converted to CW in heptanoic acid suggesting that the CW pattern is energetically more favorable.

Table 2: Geometrical parameters of optimized CW structures on bilayer graphite.

CW	A, B, γ	α	E_{ads} (eV)	ΔE_{bind} (eV)	-O-H \cdots O- (Å)
CW ₁₀	25.02, 25.02, 60.0°	9.9°	-4.1047	-0.6685	2.28
CW ₀	24.59, 24.59, 60.0°	0.0°	-4.0317	-0.6408	1.74
Expt.	25.0, 25.0, 60°	$\approx 0^\circ$			

S4: Time dependent STM topographs of L-BTA monolayer at HOPG-heptanoic acid interface.

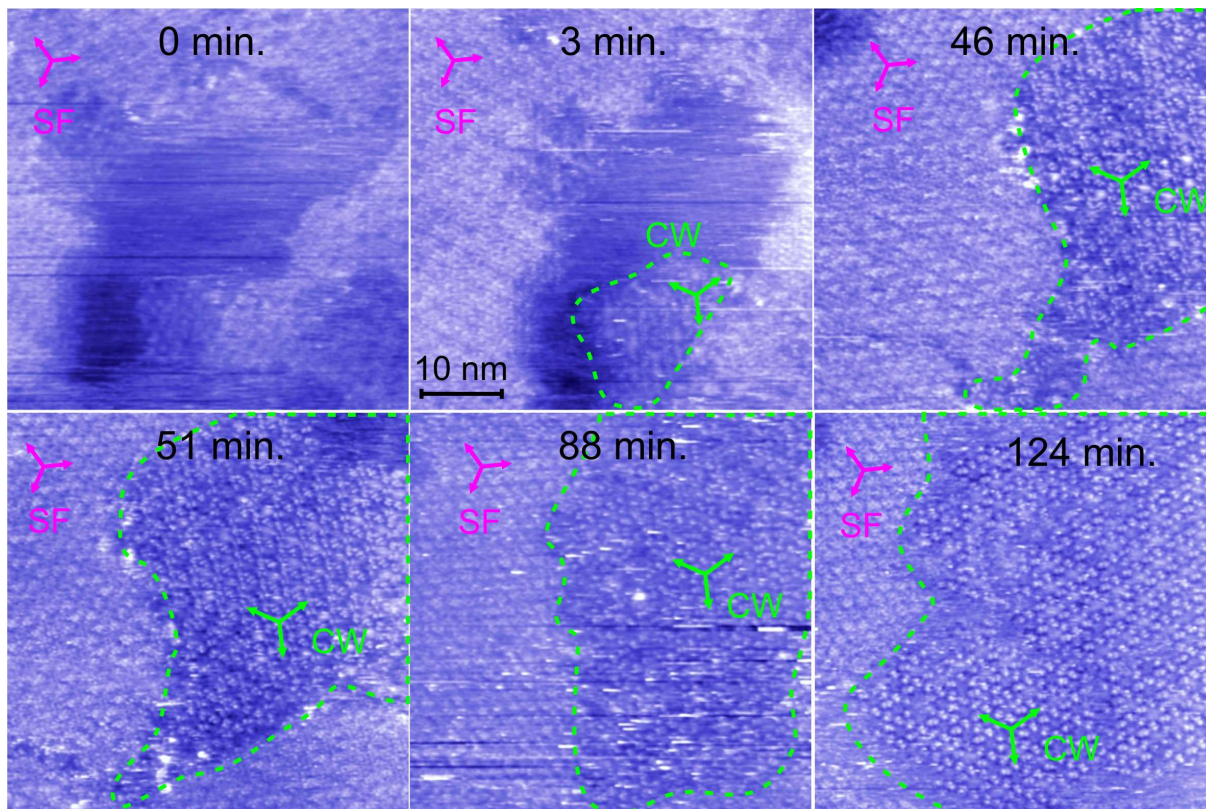


Figure 8: Time dependent STM topographs (0.5 V and 40 pA) of L-BTA monolayer at HOPG-heptanoic acid interface. The time interval between the images is indicated in the corresponding image. Green dashed line indicates the domain of CW pattern, which is growing as time progress. The remaining region in the frames is SF structure. Three-fold magenta and green arrows indicate the lattice orientation of SF and CW structures, respectively.

S5: Geometry of L-BTA in SF and CW structures.

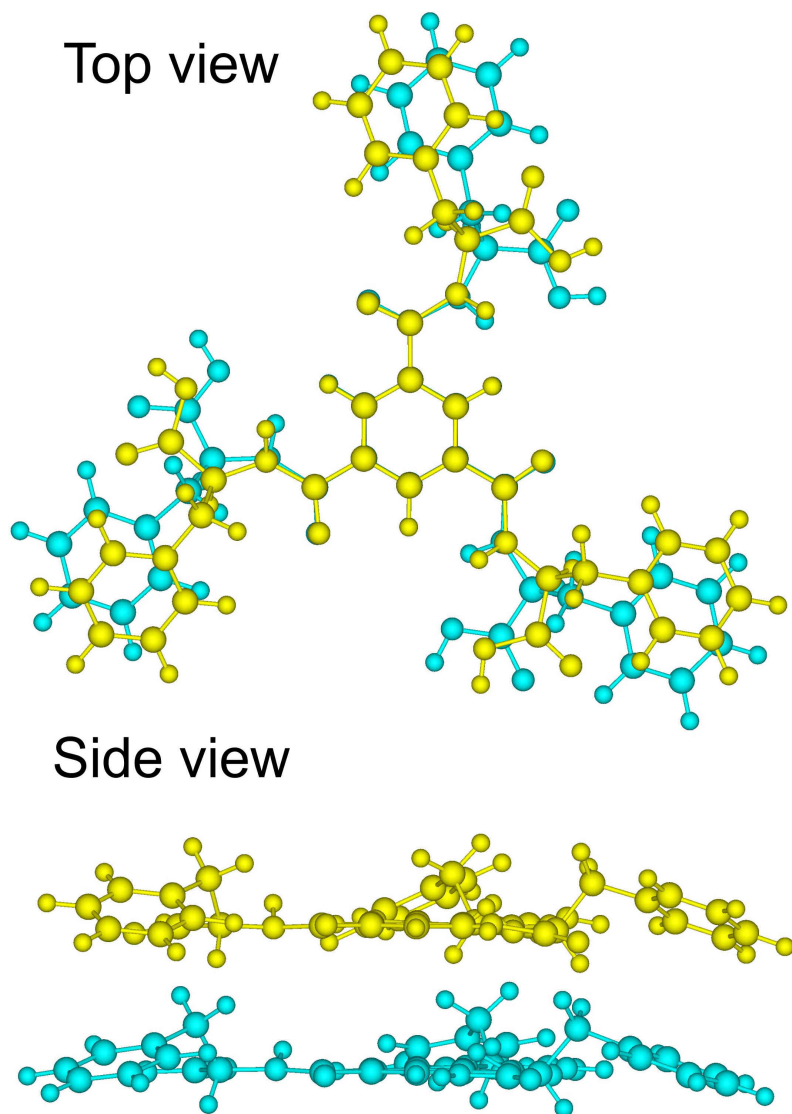


Figure 9: Optimized geometry (top and side view) of L-BTA in SF (yellow) and CW (blue) structures overlaid. The conformation of L-BTA within SF and CW structures are geometrically comparable with minor changes in the relative orientation of the groups.

S6: STM topograph of SF structure observed at HOPG-nonanoic acid interface.

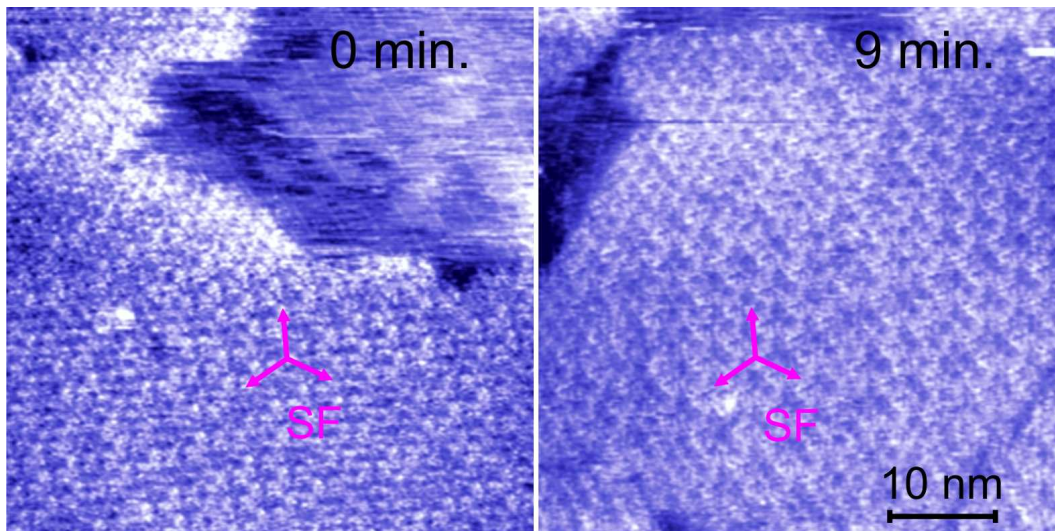


Figure 10: STM topographs (0.5 V and 40 pA) of SF structure observed at HOPG-nonanoic acid interface. Nearly saturated solution of L-BTA in nonanoic acid is used. The time interval between the images is indicated in the corresponding image. Three-fold magenta arrows indicate the lattice orientation of SF pattern.

S7: Time dependent STM topograph of L-BTA monolayer at HOPG-nonanoic acid interface.

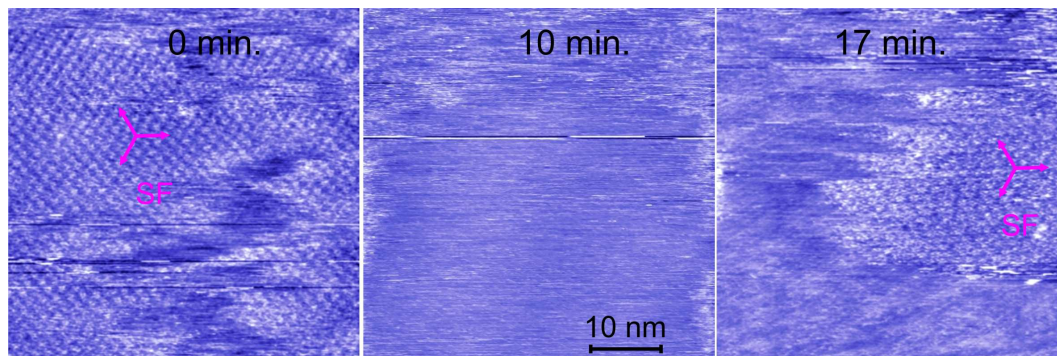


Figure 11: Time dependent STM topographs (0.5 V and 40 pA) of SF structure observed at HOPG-nonanoic acid interface. The time interval between the images is indicated in the corresponding image. Three-fold magenta arrows indicate the lattice orientation of SF pattern. During the scanning, independent of the concentration used, we observed domains of SF structure are rearranging, vanishing and reappearing.

S8: Van't Hoff plots of the solubility of L-BTA as a function of temperature

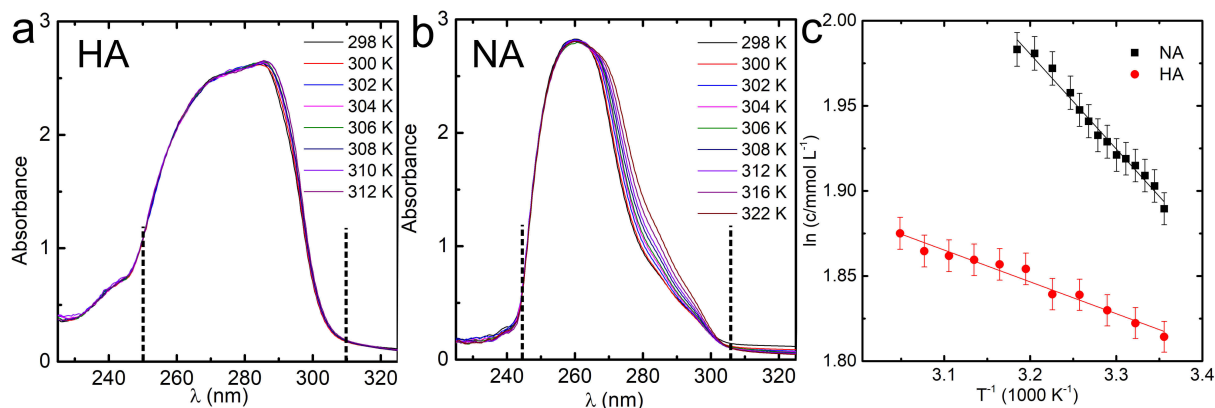


Figure 12: UV-Vis spectra of L-BTA in heptanoic acid (HA) (a) and nonanoic acid (NA)(b) as a function of temperature. A saturated solution with small amount of sediments are used for the experiment. The concentration corresponding to each temperature is measured by integrating the absorbance within the indicated range (dashed vertical lines) of wavelengths and comparison with pre-calibrated standard concentrations. (c) Van 't Hoff plots for the solubility of BTA as a function of temperature in HA and NA. The slope of the plot corresponds to the dissolution enthalpy (ΔH) of BTA in the respective solvent and the intercept corresponds to the standard dissolution entropy (ΔS°). $\Delta H_{HA} = 1.55 \text{ kJ/mol}$; $\Delta H_{NA} = 4.83 \text{ kJ/mol}$; $\Delta S_{HA}^\circ = 20.30 \text{ J/mol/K}$ and $\Delta S_{NA}^\circ = 31.93 \text{ J/mol/K}$.

S9: Concentration dependent UV-vis spectra of L-BTA in different solvents.

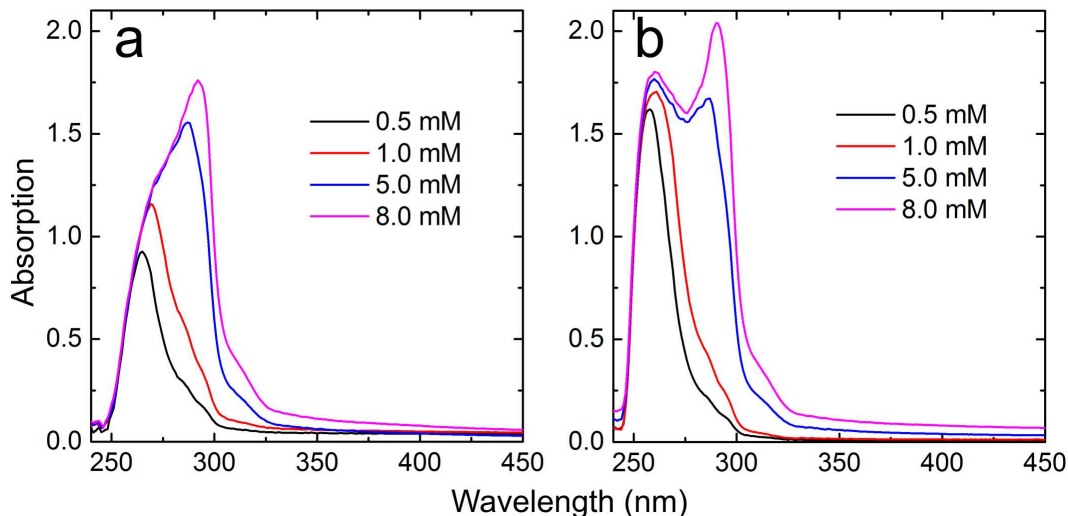


Figure 13: UV-Vis spectra as a function of concentration for L-BTA in HA (a) and NA (b). If L-BTA forms aggregates (helical aggregates) within the solvents, an overall blue shift or broadening with emergence of new bands is expected in the UV-vis spectra.^{4,5} The UV-vis spectra recorded at 5 and 8 mM show substantial broadening with emergence of a new band. These concentrations correspond to the limiting solubility. We attribute the effect at higher concentration is due to the formation of aggregates in the solution. For lower concentrations no such effect is observed. To further confirm the formation of aggregates in the solution, we have performed dynamic light scattering (DLS) experiment of L-BTA dissolved in HA and NA at different concentrations (0.5 mM and 6 mM). No aggregates/particles are observed at lower concentration (0.5 mM) for L-BTA in both solvents. However, for higher concentration (6 mM), particles with effective diameter ranging from 25-48 μm and 3-122 μm are observed for heptanoic acid and nonanoic acid, respectively. We presume that these are aggregates of L-BTA as reported earlier. That is, the concentration at which we perform the experiments at solid-liquid interface ($\sim 10^{-4}$ to 10^{-3} M), the possibility of aggregation of L-BTA within the solution is minimal. Thus, we conclude that L-BTA molecules are molecularly dissolved in the solvents during the solid-liquid interface experiments.

References

- (1) Zhu, C.; Tang, H.; Yang, K.; Fang, Y.; Wang, K.-Y.; Xiao, Z.; Wu, X.; Li, Y.; Powell, J. A.; Zhou, H.-C. Homochiral Dodecanuclear Lanthanide “Cage in Cage” for Enantioselective Separation. *J. Am. Chem. Soc.* **2021**, *143*, 12560–12566.
- (2) Schneider, J.; Hamaekers, J.; Chill, S. T.; Smidstrup, S.; Bulin, J.; Thesen, R.; Blom, A.; ; Stokbro, K. ATK-ForceField: a new generation molecular dynamics software package. *Modelling Simul. Mater. Sci. Eng.* **2017**, *25*, 085007.
- (3) Badami-Behjat, A.; Deimel, P. S.; Allegretti, F.; Ringel, E.; Mahata, K.; Schmittl, M.; Barth, J. V.; Heckl, W. M.; Lackinger, M. Versatile Role of Molecule-Surface Interactions for Monolayer Self-Assembly at Liquid-Solid Interfaces: Substrate-Induced Polymorphism, Thermodynamic Stability, and New Polymorphs. *Chem. Mater.* **2022**, *34*, 8876–8884.
- (4) Terashima, T.; Mes, T.; Greef, T. F. A. D.; Gillissen, M. A. J.; Besenius, P.; Palmans, A. R. A.; Meijer, E. W. Single-Chain Folding of Polymers for Catalytic Systems in Water. *J. Am. Chem. Soc.* **2011**, *133*, 4742–4745.
- (5) Matsumoto, N. M.; Lafleur, R. P. M.; Lou, X.; Shih, K.-C.; Wijnands, S. P. W.; Guibert, C.; van Rosendaal, J. W. A. M.; Voets, I. K.; Palmans, A. R. A.; Lin, Y. et al. Polymorphism in Benzene-1,3,5-tricarboxamide Supramolecular Assemblies in Water: A Subtle Trade-off between Structure and Dynamics. *J. Am. Chem. Soc.* **2018**, *140*, 13308–13316.